RSC Advances

PAPER

View Article Online
View Journal | View Issue

Cite this: *RSC Adv.*, 2026, **16**, 9027

Phenylboronic acid modified Ag_2S NPs for bacterial targeting photothermal antibacterial therapy and promotion of wound healing

Yixiang HePeng,†[a] Zhi Xu,†[bc] Ping Gou,†[d] Bosong Zhou,[a] Quan Zheng,[a] Ke Zhu,[bc] Xiangfeng Liu,[bc] Ruiyuan Liu,*[e] Xu Wu*[ab] and Chao Zhang*[fg]

Photothermal therapy is an antibacterial strategy based on the photothermal conversion effect, characterized by rapid action and a low tendency for resistance. However, traditional photothermal materials often lack the ability to specifically target bacteria, which limits their precise bactericidal efficacy in complex infection environments. A nanoplatform integrating photothermal therapy and targeted antibacterial action, composed of the targeting fragment 4-carboxyphenylboronic acid, photothermal agent Ag_2S, and stabilizer phycocyanin (PBA-Ag_2S@PC NPs), has been successfully established. The experimental results indicate that PBA-Ag_2S@PC NPs exhibit exceptional photothermal conversion capabilities and demonstrate targeted antibacterial effects, enhanced by photothermal action, against *Staphylococcus aureus* and *Escherichia coli*. Both *in vitro* and *in vivo* tests confirm the excellent biocompatibility of PBA-Ag_2S@PC NPs and their potential to promote wound healing. Overall, the constructed PBA-Ag_2S@PC NPs represent an efficient targeted photothermal antibacterial nanoplatform, demonstrating significant potential for promoting the repair of infected wounds.

Received 20th December 2025
Accepted 9th February 2026

DOI: 10.1039/d5ra09845a

rsc.li/rsc-advances

1 Introduction

Bacterial infection is one of the most common complications during the healing process of skin wounds and has become a significant threat to human health.[1,2] Antibiotics represent one of humanity's greatest inventions, saving countless lives throughout history.[3] However, with the increasing issues related to antibiotic misuse and resistance, traditional antibiotic therapies are no longer sufficient to meet current clinical treatment demands.[4–6] Therefore, the development of novel antibacterial strategies has become particularly urgent.

Photothermal therapy (PTT) is a novel antibacterial strategy characterized by its broad-spectrum photothermal antimicrobial properties.[7,8] Under near-infrared light irradiation, it efficiently converts absorbed light energy into hyperthermia, achieving effective sterilization while minimizing the risk of bacterial resistance development.[9,10] Metal sulfide nanomaterials, such as Ag_2S, CuS, and MnS, exhibit high absorption rates and photothermal conversion efficiencies in the near-infrared (NIR) region.[11–15] They also offer advantages including low cost, ease of preparation, and high stability.[16,17] Consequently, these materials have garnered significant attention in the field of photothermal antibacterial therapy. However, the application model of PTT therapy is singular and limited, lacking targeted selectivity towards bacteria.[18–20] This results in non-specific cytotoxicity to normal tissue cells and low bactericidal efficiency. To further enhance the antibacterial effect, it is of significant importance to develop antimicrobial nanomaterials with bacterial targeting properties.

Phenylboronic acid (PBA), as a small molecule ligand, is characterized by its low cytotoxicity and ease of modification.[21–24] By utilizing the boronic acid group, covalent bonds can be formed with the polysaccharides on the surface of bacteria, thereby enabling targeted delivery to bacterial cells and enhancing accumulation at the bacterial membrane. Leveraging the unique affinity of PBA for polysaccharides on bacterial surfaces, researchers have incorporated it as a key targeting moiety into nanocarrier design. For example, Wang *et al.* designed mercaptophenylboronic acid (MBA)-modified

[a]*Department of Thoracic Surgery, Nanfang Hospital, Southern Medical University, Guangzhou, 510515, China. E-mail: wuxu_southhospital@163.com*

[b]*Huiqiao Medical Center, Nanfang Hospital, Southern Medical University, Guangzhou, 510515, China*

[c]*Department of General Practice, Nanfang Hospital, Southern Medical University, Guangzhou, 510515, China*

[d]*Department of Medicine Ultrasonics, Nanfang Hospital, Southern Medical University, Guangzhou, 510515, China*

[e]*Biomaterials Research Center, School of Biomedical Engineering, Southern Medical University, Guangzhou, 510515, China. E-mail: ruiyliu@smu.edu.cn*

[f]*Experimental Education/Administration Center, National Demonstration Center for Experimental Basic Medical Education, School of Basic Medical Science, Southern Medical University, Guangzhou, 510515, China. E-mail: super1998@smu.edu.cn*

[g]*Department of Biochemistry and Molecular Biology, School of Basic Medical Science, Southern Medical University, Guangzhou, 510515, China*

† These three authors contributed equally to this work.

gold nanoclusters ($Au_{44}(MBA)_{18}$) that targeted and effectively killed vancomycin-resistant *Enterococcus faecalis*.[25] Wang *et al.* developed phenylboronic acid-functionalized silver nanoparticles (AgNPs-PBAn) that target *E. coli* in infected wounds and release antibacterial Ag^+ ions, enabling precise, efficient treatment and rapid wound healing.[26] Liu *et al.* prepared a carrier-free antibacterial nanodrug (NEP NPs) *via* PBA, epigallocatechin-3-gallate (EGCG),and self-assembly of nitrofural (NIT) for targeted therapy of subcutaneous *S. aureus*-induced skin infection.[27] This strategy successfully confered active targeting capability and enabled selective accumulation within bacterial biofilms, thereby significantly enhancing the precision and delivery efficiency of antimicrobial agents at infection sites. Building upon precise bacterial targeting, multifunctional nanoplatforms that integrate additional synergistic antibacterial mechanisms have gradually emerged as a research hotspot in the field of antibacterial drug delivery systems. For example, Liu *et al.* developed phenylboronic acid-functionalized BSA@CuS@PpIX NPs, which exhibit selective targeting toward *S. aureus* and *E. coli*, enabling synergistic antibacterial PDT/PTT for enhanced therapeutic efficacy.[28] Li *et al.* engineered PdSAs@GSH NPs through atomic-level modification of palladium single atoms (PdSAs) with glutathione (GSH) and mercaptophenylboronic acid (MBA), which demonstrated excellent targeted photothermal antibacterial activity against *E. coli* under 808 nm NIR laser irradiation and effectively promoted wound healing in a rat infection model.[29]

Phycocyanin (PC), a natural water-soluble protein, exhibits biological safety, non-immunogenicity, and serves as a stabilizer for nanoparticles. For example, phycocyanin can be utilized to modify metal or non-metal nanoparticles such as Se NPs, CuS NPs, and PDA NPs, which are widely applied in the biomedical field.[30–34] PC is amenable to chemical modification owing to its peptide backbone. Owing to its peptide backbone, which is rich in amino and carboxyl groups, PC is amenable to precise chemical modifications that generate novel structural derivatives, such as upconversion nanoparticle–conjugated PC (PC-UCNPs),[35] PEGylated PC,[36] and glycation-modified PC (MPC).[37] Moreover, phycocyanin exhibits remarkable potential in promoting wound healing.[38–42]

Therefore, the modification of Ag_2S NPs using bacterial-targeting fragment PBA and phycocyanin, which integrates targeted antibacterial activity with photothermal therapy, is expected to emerge as an effective strategy for wound healing. In this study, we have rationally designed and conveniently generated a bacterial-targeted photothermal antibacterial nanoparticles, PBA-Ag_2S@PC NPs (Scheme 1A), by loading 4-carboxyphenylboronic acid (4-CPBA) onto phycocyanin-stabilized Ag_2S NPs. The utilization of PC as a carrier matrix for Ag_2S NPs (photothermal agent) significantly enhances their

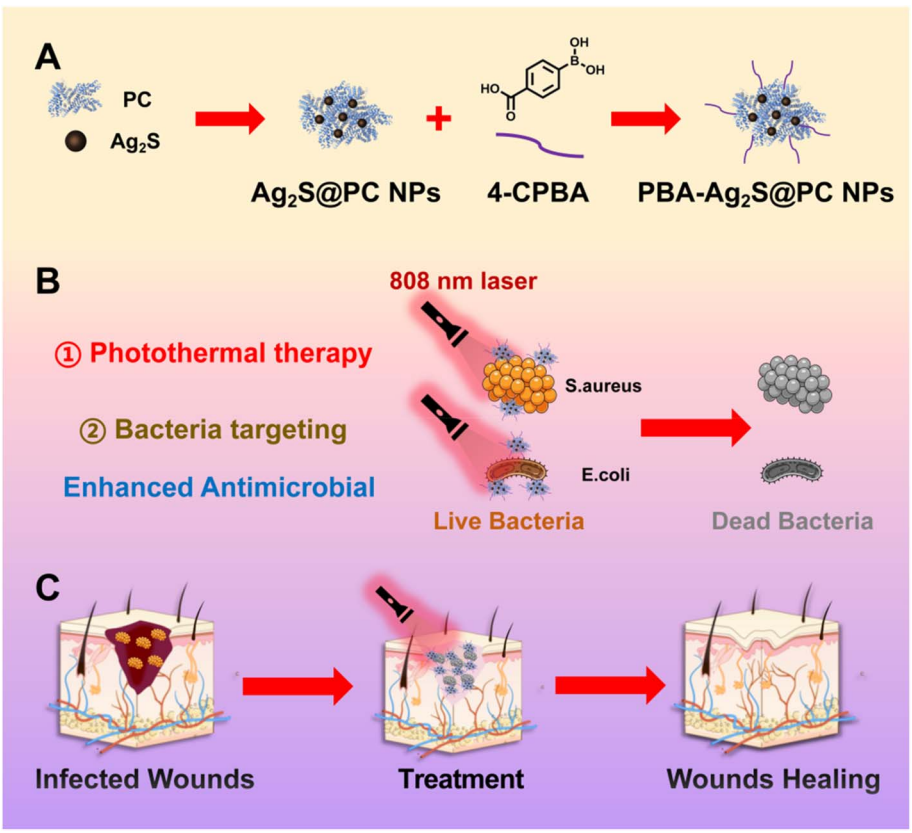

Scheme 1 Diagram the preparation procedure and antimicrobial mechanism of as-established PBA-Ag_2S@PC NPs. (A) Synthesis strategy and assembly process for the construction of PBA-Ag_2S@PC NPs. (B) PBA-mediated bacteria targeting and combined antibacterial PTT of PBA-Ag_2S@PC NPs. (C) Biological application of PBA-Ag_2S@PC NPs for bacteria targeting and PTT therapy toward bacterial infection.

nano-stability and biocompatibility. 4-CPBA is introduced as a bacterial targeting moiety to greatly facilitate the interaction between PBA-Ag_2S@PC NPs and bacteria. The combination of targeted bacteria and photothermal therapy substantially increases the antibacterial efficacy (Scheme 1B). The experimental results indicate that this technology can effectively promote wound healing at the site of infection (Scheme 1C). This approach offers a non-antibiotic bactericidal method for the repair of infectious wounds.

2 Materials and methods

2.1. Materials

Phycocyanin (C-PC), sodium sulfide nonahydrate (Na_2S), *N*-hydroxysuccinimide (NHS), 4-carboxyphenylboronic acid (4-CPBA) were obtained from Macklin (China). Silver nitrate ($AgNO_3$) was obtained from Juyansi (Guangzhou) Chemical Co., Ltd (China). (3-Dimethylaminopropyl)-3-ethylcarbodiimide hydrochloride (EDC) was obtained from Aladdin (China). The L929 cell line was obtained from the Shanghai Cell Bank of the Type Culture Collection at the Chinese Academy of Sciences. Cell culture reagents, including Minimum Essential Medium (MEM), penicillin G (100 U mL^{-1}), streptomycin (100 U mL^{-1}), and a 0.25% trypsin-0.53 mM EDTA solution, were purchased from Gibco (Grand Island, USA). Horse serum was supplied by iCell Bioscience Inc. (China). *S. aureus* and *E. coli* were provided by Nanfang Hospital in China. The CCK-8 assay kit was purchased from Dojindo Co., Ltd. in Japan. The SYTO9-PI Live/Dead Bacteria Stain Kit was purchased from Tianjingsha (China). Fluorescein isothiocyanate, hematoxylin-eosin staining kit and Masson three-color staining solution were obtained from Solarbio (China).

2.2. Synthesis and characterization of Ag_2S@PC NPs and PBA-Ag_2S@PC NPs

The Ag_2S@PC NPs were prepared using PC as a stabilizing agent. First, 250 mg of PC was added to 8 mL of pure water, followed by the gradual addition of 1 mL of 0.2 mM $AgNO_3$ solution until the system became turbid. Subsequently, 1 mL of 0.1 M NaOH solution was introduced to adjust the pH to an alkaline level. Finally, 18.2 mg of Na_2S was added to the mixture. After stirring at 55 °C for 4 hours, a solution containing $A_{g2}S$@PC NPs was obtained. The preparation of PBA-Ag_2S@PC NPs involves the simultaneous addition of a 1 mL DMSO solution containing 44 mg 4-CPBA, 25.2 mg of NHS and 64 mg of EDC during the aforementioned reaction.

2.3. Evaluation of photothermal properties

The PBA-Ag_2S@PC NPs aqueous dispersion solutions with concentrations of 0, 50, 100, 150, and 200 μg mL^{-1} were added to a cuvette and irradiated with a laser at a wavelength of 808 nm and an intensity of 2.0 W cm^{-2} for a duration of 10 minutes. Additionally, the aqueous dispersion solution containing PBA-Ag_2S@PC NPs at a concentration of 200 μg mL^{-1} was added to a cuvette and subjected to irradiation using lasers with intensities of 0.5, 1.0, 1.5, 2.0 and 2.5 W cm^{-2} for a duration of 10 minutes. Furthermore, the aqueous dispersion solution containing PBA-Ag_2S@PC NPs at a concentration of 200 μg mL^{-1} was exposed to an intensity of 2.0 W cm^{-2} from 808 nm laser for a period of 30 minutes. The absorption peak characteristics were analyzed through UV-vis-NIR spectroscopy. Throughout these experiments, temperature variations were monitored and recorded using a Fluke TiS20 infrared thermal imager during each cycle (comprising heating for 10 minutes followed by cooling for 10 minutes). All experiments were conducted in triplicate. The photothermal conversion efficiency was determined by monitoring the temperature change of an aqueous dispersion of PBA-Ag_2S@PC NPs under continuous irradiation with an 808 nm laser (2.0 W cm^{-2}) for 600 s (t), until the solution temperature reached a steady state. The photothermal conversion efficiency (η) was calculated by equation: $\eta = [hA(T_{max} - T_{surr}) - Q_{Dis}]/[I(1 - 10^{-A_\lambda})]$.[43]

2.4. Evaluation of cytocompatibility

The L929 cells were cultured in a 96-well plate at a density of 1×10^4 cells per well. The cells were treated with varying concentrations of PBA-Ag_2S@PC NPs (0–200 μg mL^{-1}). After a 24 hours incubation period, 100 μL of CCK-8 reagent was added to each well and incubated for an additional 2 hours. The absorbance at A_{450nm} was measured using a multifunctional microplate reader, and the cell viability for each group was calculated accordingly.

2.5. Evaluation of hemocompatibility

The venous blood samples from SD rats were centrifuged at 1500 rpm for 15 minutes to obtain red blood cells. A total of 50 μL of a 5% red blood cell solution was added to 1 mL of physiological saline and incubated with varying concentrations of PBA-Ag_2S@PC NPs (0–200 μg mL^{-1}) in a water bath at 37 °C for two hours. A 0.9% normal saline solution was used as the negative control, while distilled water served as the positive control. The supernatants were subsequently collected and analyzed using a microplate reader calibrated to an absorbance wavelength of 540 nm. The hemolysis ratio of red blood cells was calculated employing the following equation: hemolysis ratio percent $= (A_{sample} - A_{negative})/(A_{positive} - A_{negative}) \times 100\%$.

2.6. Assessment of bacterial targeting efficacy

Fluorescein isothiocyanate (FITC) was employed to label Ag_2S@PC NPs and PBA-Ag_2S@PC NPs. Specifically, 1 mL of Ag_2S@PC NPs suspension and 1 mL of PBA-Ag_2S@PC NPs suspension were each labeled with 3 μL of FITC solution. The FITC-labeled Ag_2S@PC NPs and FITC-labeled PBA-Ag_2S@PC NPs were separately co-cultured with *S. aureus* and *E. coli* solutions (10^8 CFU mL^{-1}) for 3 hours, in the presence or absence of glucose (10 μg mL^{-1}). After centrifugation and washing, observations were conducted using CLSM (excitation: 488 nm, emission: 522 nm). Bacterial uptake of Ag_2S@PC NPs and PBA-Ag_2S@PC NPs was quantitatively analyzed using flow cytometry and FlowJo software.

2.7. Evaluation of antibacterial activity

The antibacterial effects of PBA-Ag_2S@PC NPs were investigated using *S. aureus* and *E. coli*. The antibacterial efficacy was assessed through colony-forming unit (CFU) assays and SYTO9/PI live/dead staining experiments. A concentration of 200 μg mL^{-1} PBA-Ag_2S@PC NPs, along with an equivalent amount of Ag_2S@PC NPs, was co-cultured with 1 mL of *S. aureus* and *E. coli* suspension (1×10^5 CFU mL^{-1}). The treatment group subjected to laser therapy received irradiation from an 808 nm laser (2.5 W cm^{-2}) for a duration of 10 minutes. Following the treatment, the solution (100 μL) was evenly spread onto LB agar plates and incubated at 37 °C for 24 hours. In contrast, the groups that did not receive exposure to the 808 nm laser were directly incubated in a dark environment at 37 °C for the same period. The standardized bacterial viability is calculated using the following formula: bacterial viability (%) = (CFU count in the treatment group/CFU count in the control group) × 100%. At the same time, SEM was employed to observe the bacterial morphology in different treatment groups.

2.8. *In Vivo* wound healing assay

The experimental subjects consisted of 30 SPF-grade male SD rats, aged between 6 to 8 weeks and weighing between 250 to 300 grams. These animals were provided by the Animal Center of Southern Medical University. All animal experiments were conducted in accordance with the experimental protocols approved by the local ethics committee, adhering to relevant laws and regulations regarding laboratory animals in China. Additionally, these experiments followed the guidelines established by the Institutional Animal Care and Use Committee of Southern Medical University. The 30 rats were randomly divided into five groups ($n = 6$) using a random number table: NS control group, Ag_2S@PC NPs treatment group, PBA-Ag_2S@PC NPs treatment group, Ag_2S@PC NPs + PTT treatment group, and PBA-Ag_2S@PC NPs + PTT treatment group. SD rats were anesthetized *via* intraperitoneal injection of sodium pentobarbital at a concentration of 50 mg kg^{-1} in a sterile environment. A sterile punch biopsy tool with a diameter of 1.0 cm was used to create four symmetrical full-thickness skin defects (1.0 cm × 1.0 cm) on either side of the rat's spine. The four wounds on each rat received identical interventions; therefore, all statistical analyses were conducted using the individual animal as the independent experimental unit ($n = 6$ per group). Specifically, at each observation time point, the measurements from the four wounds of each rat were averaged to yield a single representative value per animal. Subsequent intergroup comparisons were performed using these animal-level mean values. Subsequently, each wound was uniformly inoculated with 200 μL of *S. aureus* suspension (1×10^8 CFU mL^{-1}). For the groups receiving PTT treatment, an 808 nm laser was applied for 10 minutes at a power density of 2.5 W cm^{-2} on days 1, 3, and 5 post-modeling. During the treatment period, nanoparticle suspensions were administered once every two days. The rats were individually housed in separate cages with dressings changed every two days. High-resolution digital photographs were taken on days 0, 3, 7, and 14 post-modeling to document wound healing progress; these images were quantitatively analyzed for wound area using IMAGEJ software. On day four post-treatment initiation, bacterial infection levels across all groups were assessed using CFU methods. Tissue specimens from the wounds were collected on days seven and fourteen after modeling for histological examination. Hematoxylin-eosin staining was employed to observe epidermal regeneration and dermal tissue structure reconstruction while Masson's trichrome staining was utilized to evaluate collagen deposition.

2.9. Statistical analysis

Statistical analysis was performed using Origin Pro 2025 software (OriginLab, Berkeley, CA, USA). Data are presented as Mean ± SD. Statistical comparisons between samples were conducted using one-way ANOVA followed by Tukey's post hoc test. A P value less than 0.05 was considered statistically significant.

3 Results and discussion

3.1. Preparation and characterization of the Ag_2S@PC NPs and PBA-Ag_2S@PC NPs

In this study, Ag_2S@PC NPs were synthesized through a one-step reaction between silver nitrate ($AgNO_3$) and sodium sulfide (Na_2S) in the presence of PC under high-temperature and alkaline conditions. As shown in Fig. S1, a color transition was observed from light ($AgNO_3$, Na_2S, and PC) to dark brown (Ag_2S@PC NPs). The synthesis of PBA-Ag_2S@PC NPs involved the activation of amino groups on phycocyanin during the aforementioned reaction, followed by the addition of 4-carboxyphenylboronic acid to modify the bacterial targeting fragment PBA onto Ag_2S@PC NPs (Fig. 1A). DLS analysis revealed that the sizes of Ag_2S@PC NPs and PBA-Ag_2S@PC NPs were approximately 81.02 ± 15.23 nm and 113.75 ± 20.51 nm, respectively (Fig. 1B and S2–S3). TEM measurements demonstrated that both Ag_2S@PC NPs and PBA-Ag_2S@PC NPs exhibited relatively clear core structures, with diameters of approximately 80 nm and 110 nm, respectively (Fig. 1C and D). As shown in the Fig. 1E, the surface potential of Ag_2S@PC NPs is measured at −16.15 ± 0.49 mV. Due to the negative charge of boric acid in the solution, the surface charge of PBA-Ag_2S@PC NPs is recorded as −20.98 ± 0.45 mV. In the entire nanosystem, the incorporation of PC significantly enhanced the stability of Ag_2S@PC NPs and PBA-Ag_2S@PC NPs. During a 7 days incubation period in physiological saline and PBS, no significant changes in size were observed (Fig. S4 and S5). The X-ray photoelectron spectroscopy (XPS) analysis further examined the elemental composition of Ag_2S@PC NPs and PBA-Ag_2S@PC NPs. Both Ag_2S@PC NPs and PBA-Ag_2S@PC NPs contain C, N, O, S, and Ag elements, each corresponding to specific peaks. Notably, PBA-Ag_2S@PC additionally exhibited a significant presence of B elements (Fig. 1F). Quantitative XPS analysis revealed that, compared with Ag_2S@PC NPs, the surface atomic concentrations of Ag and S in PBA-Ag_2S@PC NPs were slightly reduced, whereas the surface B atomic content reached 2.07%, providing direct evidence for the successful surface

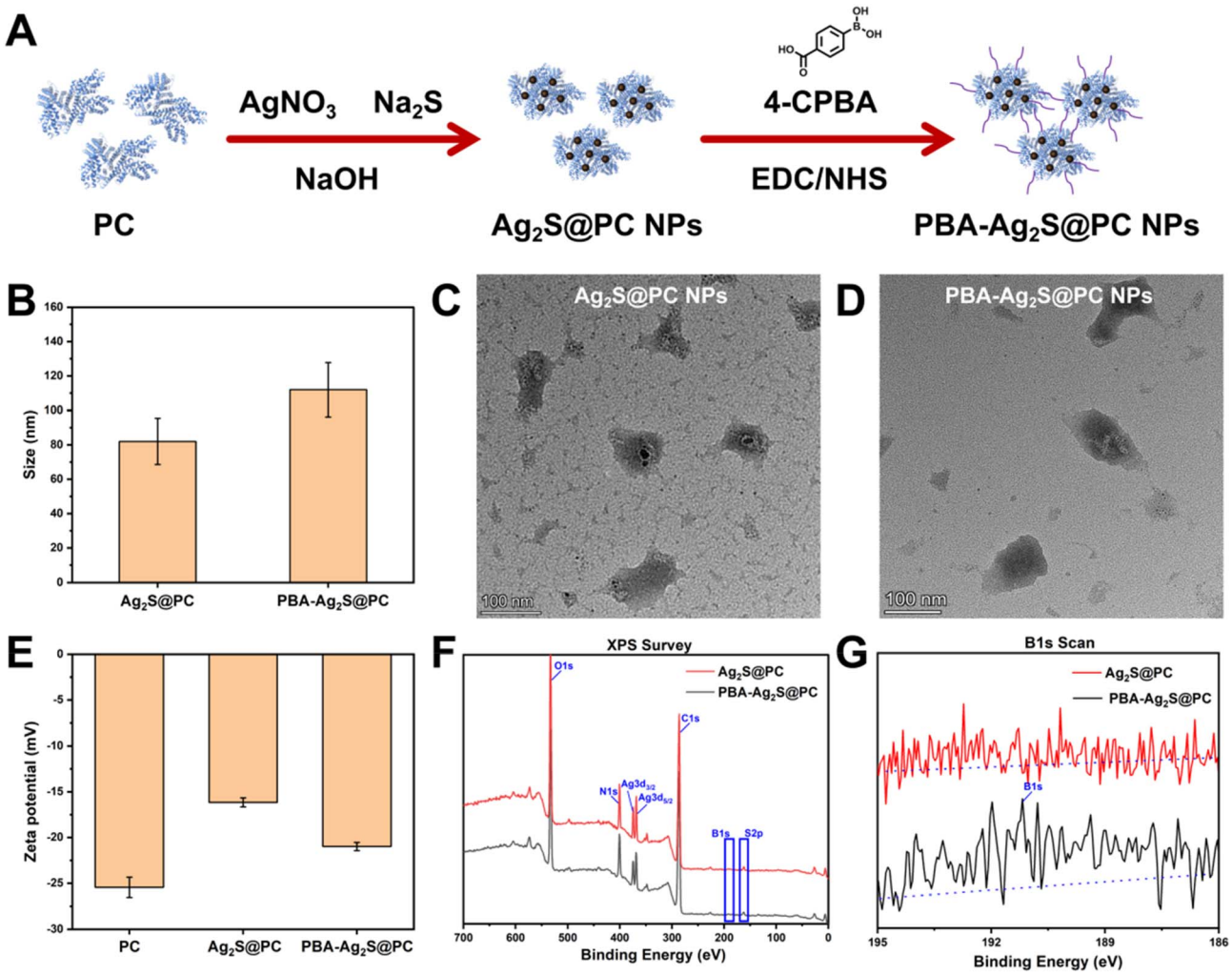

Fig. 1 The characterization of Ag_2S@PC NPs and PBA-Ag_2S@PC NPs. (A) Strategies for synthesizing Ag_2S@PC NPs and PBA-Ag_2S@PC NPs. (B) The DLS of as-prepared Ag_2S@PC NPs and PBA-Ag_2S@PC NPs ($n = 3$). (C and D) The TEM of Ag_2S@PC NPs and PBA-Ag_2S@PC NPs. (E) Zeta potential of PC, Ag_2S@PC NPs, and PBA-Ag_2S@PC NPs ($n = 3$). (F and G) The XPS spectrum of Ag_2S@PC NPs and PBA-Ag_2S@PC NPs.

functionalization of the nanoparticles with PBA (Table S1). The Fourier transform infrared spectroscopy (FT-IR) shows strong peaks at 2920 cm^{-1} and 1156 cm^{-1}, corresponding to the C–H bonds and C–O–C vibrations of sugar units in glycosidic linkages, indicating successful incorporation of PC. Additionally, we observe phenyl-related bonds at 852 cm^{-1} and B–O–H bending at 1020 cm^{-1}. These characteristic peaks confirmed that PBA has been successfully deposited on Ag_2S@PC NPs (Fig. S6). All the results presented that Ag_2S@PC NPs have been successfully synthesized, and 4-CPBA has been effectively modified onto the surface of Ag_2S@PC NPs.

3.2. Photothermal performance of PBA-Ag_2S@PC NPs

As a novel PTT agent, the photothermal properties of PBA-Ag_2S@PC NPs was investigation. As the concentration of PBA-Ag_2S@PC NPs increases, the UV-vis-NIR spectra of PBA-Ag_2S@PC NPs exhibit a gradual rise in absorbance within the NIR region from 500 to 900 nm. This observation indicates that PBA-Ag_2S@PC NPs possess a commendable capacity for near-infrared absorption (Fig. S7). The 808 nm laser with a power density of 2.0 W cm^{-2} was used to irradiate aqueous solutions of PBA-Ag_2S@PC NPs at different concentrations (0, 50, 100, 150, and 200 μg mL^{-1}) for a duration of 10 minutes. The results indicated that both the heating rate and the maximum stable temperature increased with higher concentrations (Fig. 2A). Additionally, when the same aqueous solution of PBA-Ag_2S@PC NPs (200 μg mL^{-1}) was exposed to an 808 nm laser at varying power densities (0.5, 1.0, 1.5, 2.0 and 2.5 W cm^{-2}) for a period of 10 minutes, it was observed that the heating rate and maximum stable temperature also rose in accordance with increasing laser power (Fig. 2B). Further exposure of equal amounts of Ag_2S@PC NPs and PBA-Ag_2S@PC NPs to an 808 nm laser at a power density of 2.5 W cm^{-2} for 10 minutes confirmed that the modification with 4-CPBA in PBA-Ag_2S@PC NPs does not significantly hinder the PTT effect (Fig. 2C). The thermal imaging diagram of the PBA-Ag_2S@PC NPs aqueous solution indicated that, after being irradiated with a 808 nm laser (2.5 W cm^{-2}) for 10 minutes, the temperature increased rapidly from 30.0 to 52.2 °C, resulting in a temperature elevation of 22.2 °C (Fig. 2D). A comparison of the absorption spectra of

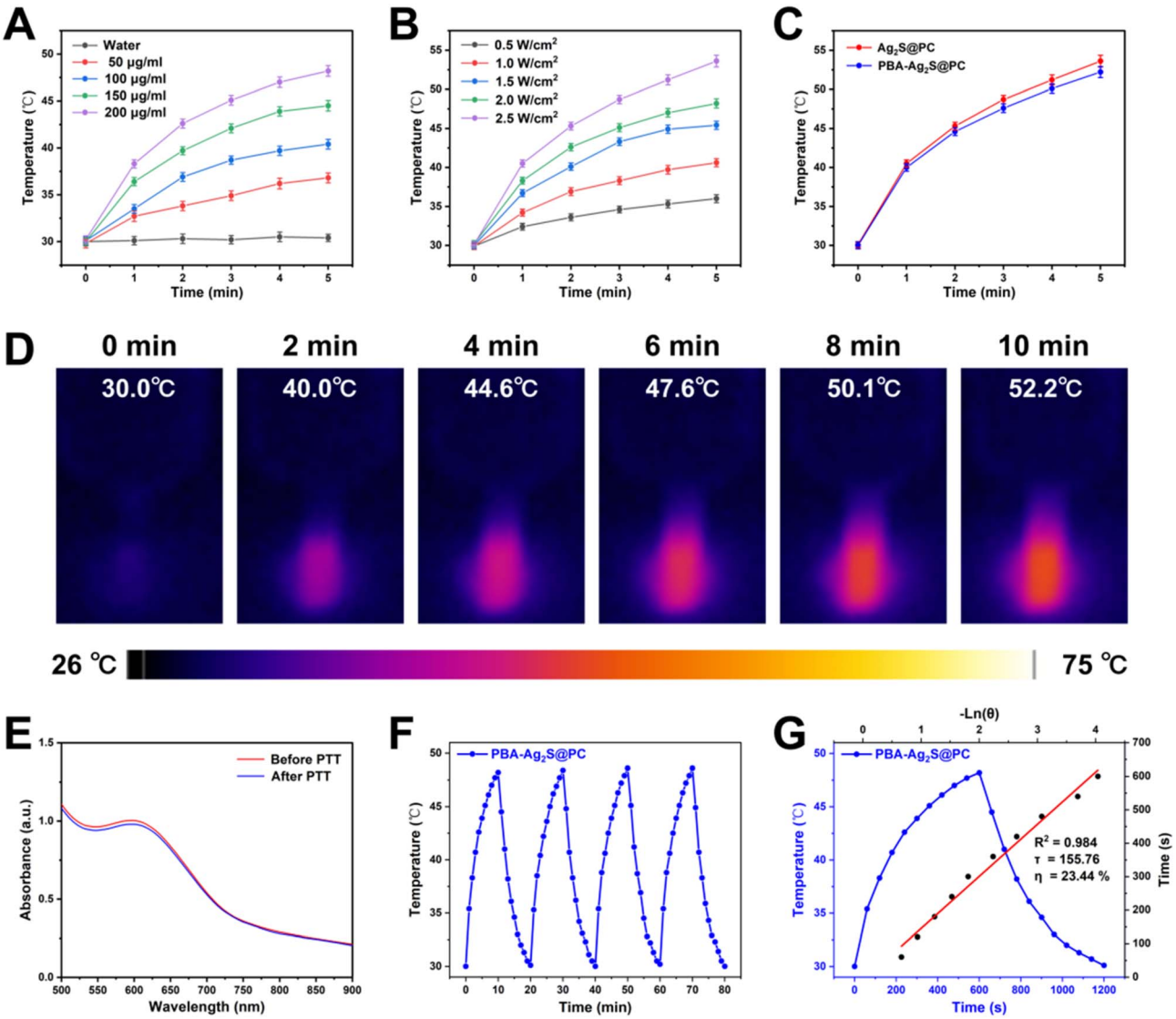

Fig. 2 The photothermal properties of Ag_2S@PC NPs. (A) Temperature curves of different concentration of Ag_2S@PC NPs concentrations under 808 nm laser irradiation at 2.0 W cm^{-2} ($n = 3$). (B) Temperature curves of 200 μg mL^{-1} Ag_2S@PC NPs under 808 nm laser irradiation at different power levels ($n = 3$). (C) Photothermal properties of equal amounts of Ag_2S@PC NPs and PBA-Ag_2S@PC NPs upon 808 nm laser irradiation (2.5 W cm^{-2}) ($n = 3$). (D) *In vitro* photothermal images of PBA-Ag_2S@PC NPs. (E) UV-vis absorption of PBA-Ag_2S@PC NPs under 808 nm laser irradiation for 30 minutes (2.0 W cm^{-2}). (F) Thermostability of PBA-Ag_2S@PC NPs exposed to 808 nm laser (2.0 W cm^{-2}) for four on/off cycles. (G) Photothermal conversion profiles of PBA-Ag_2S@PC NPs.

PBA-Ag_2S@PC NPs before and after exposure to 808 nm laser (2.0 W cm^{-2}) for 30 minutes revealed no significant decrease (Fig. 2E). During the process involving four cycles of laser irradiation and shutdown, there were no significant differences in the maximum temperatures achieved across each cycle (Fig. 2F). The photothermal conversion efficiency of PBA-Ag_2S@PC NPs was calculated to be 23.44% (Fig. 2G). This indicates that PBA-Ag_2S@PC NPs possess moderate photothermal conversion efficiency and photothermal stability.

3.3. The biocompatibility of PBA-Ag_2S@PC NPs

Before conducting *in vivo* experiments, the cytotoxicity and biocompatibility of PBA-Ag_2S@PC NPs were evaluated. The results from the CCK-8 assay indicated that after co-culturing L929 cells with PBA-Ag_2S@PC NPs for 24 hours, cell viability remained above 90% across a concentration range of 0 to 200 μg mL^{-1} (Fig. 3A). Subsequently, hemolysis tests were performed to assess the blood compatibility of PBA-Ag_2S@PC NPs. As shown in Fig. 3B, the hemolysis rate (HR) at concentrations ranging from 0 to 200 μg mL^{-1} was consistently below 5%, comparable to that of the negative control group using 0.9% NS (Fig. 3B). These findings demonstrate that PBA-Ag_2S@PC NPs possess excellent cellular and blood compatibility.

3.4. *In vitro* antibacterial effect of PBA-Ag_2S@PC NPs

Considering the targeted binding affinity of PBA-Ag_2S@PC NPs to bacteria and their excellent photothermal properties, we further evaluated their broad-spectrum antibacterial activity

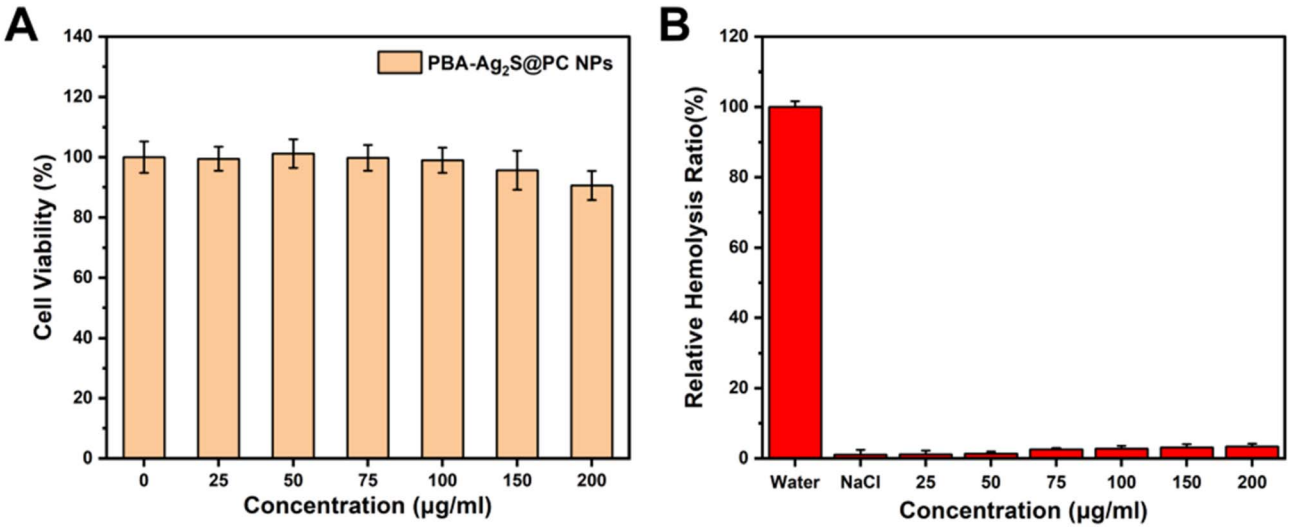

Fig. 3 (A) Cell viability of L929 cells treated with PBA-Ag_2S@PC NPs at different concentrations for 24 h ($n = 3$). (B) The blood compatibility of PBA-Ag_2S@PC NPs ($n = 3$).

against *S. aureus* and *E. coli*. To assess the bacterial targeting capability of PBA-Ag_2S@PC NPs, FITC-labeled Ag_2S@PC NPs and FITC-labeled PBA-Ag_2S@PC NPs were co-incubated with bacteria for observation. Notable green fluorescence was detected within *S. aureus* and *E. coli* treated with FITC-labeled PBA-Ag_2S@PC NPs, whereas no significant green fluorescence was observed in the control group or the FITC-labeled Ag_2S@PC NPs group (Fig. 4A and B). Since glucose can competitively form boronate ester bonds with PBA, thereby inhibiting the binding of PBA-Ag_2S@PC NPs to bacteria, we introduced glucose into the co-incubation system to block the PBA-mediated targeting capability for comparative validation. Results showed that, in the presence of glucose, the green fluorescence intensity of FITC-labeled PBA-Ag_2S@PC NPs co-incubated with *S. aureus* and *E. coli* was significantly reduced. This observation was further confirmed by quantitative flow cytometry analysis (Fig. 4C and D), which yielded results consistent with those obtained by CLSM. This effectively demonstrates the targeted binding ability of PBA-Ag_2S@PC NPs towards bacteria. The photothermal antibacterial properties of Ag_2S@PC NPs and PBA-Ag_2S@PC NPs were subsequently evaluated. Under dark conditions, both Ag_2S@PC NPs and PBA-Ag_2S@PC NPs exhibited certain antibacterial effects against the two bacterial strains, with PBA-Ag_2S@PC NPs demonstrating superior efficacy compared to Ag_2S@PC NPs. However, following exposure to an 808 nm laser, the antibacterial effects of both Ag_2S@PC NPs and PBA-Ag_2S@PC NPs were significantly enhanced; notably, the effect of PBA-Ag_2S@PC NPs was markedly amplified, achieving an antibacterial rate exceeding 95% (Fig. 4E–H). The live/dead bacterial staining using SYTO9/PI further corroborated these findings. Under photothermal conditions, compared to the control group, groups treated with Ag_2S@PC NPs and PBA-Ag_2S@PC NPs displayed increased red fluorescence intensity, with the best results observed in the group treated with PBA-Ag_2S@PC NPs (Fig. S8). Additionally, scanning electron microscopy (SEM) analysis post-exposure to the 808 nm laser revealed significant morphological changes in bacterial cells. Both Ag_2S@PC NPs and PBA-Ag_2S@PC NPs demonstrated pronounced structural damage to bacteria (Fig. 4I and J). These findings underscore the exceptional photothermal antibacterial performance of PBA-Ag_2S@PC NPs along with their targeted antibacterial capabilities mediated by PBA.

3.5. *In vivo* wound healing in a skin model with wound infection

Given that PBA-Ag_2S@PC NPs exhibit strong antibacterial activity *in vitro*, we established a rat wound infection model to investigate their *in vivo* antibacterial efficacy and ability to promote wound healing. The rats were randomly divided into five groups ($n = 6$): NS control group, Ag_2S@PC NPs treatment group, PBA-Ag_2S@PC NPs group, Ag_2S@PC NPs + PTT treatment group, and PBA-Ag_2S@PC NPs + PTT treatment group. Four full-thickness skin defects with a diameter of 10 mm were created on the back of each rat, and each defect was uniformly inoculated with 200 μL of *S. aureus* (10^8 CFU mL^{-1}). For the group receiving PTT treatment, 808 nm laser irradiation (2.5 W cm^{-2}) was administered for a duration of 5 minutes on days 1, 3, and 5. Before treatment, the *in vivo* photothermal therapeutic effect of PBA-Ag_2S@PC NPs was first monitored using thermal imaging technology. As shown in Fig. 5A, under 10 minutes of near-infrared laser irradiation, the application of PBA-Ag_2S@PC NPs to infected wounds resulted in a maximum temperature increase up to 54.3 °C. This indicates that PBA-Ag_2S@PC NPs can achieve a favorable photothermal efficacy during *in vivo* therapy. Meanwhile, no obvious extensive tissue necrosis, erythema, edema, or exudation—typical pathological manifestations—was observed at the wound sites in the animals throughout the treatment period. Next, wound samples from each group of rats were collected at various time points during the treatment, and the size of the wounds was systematically

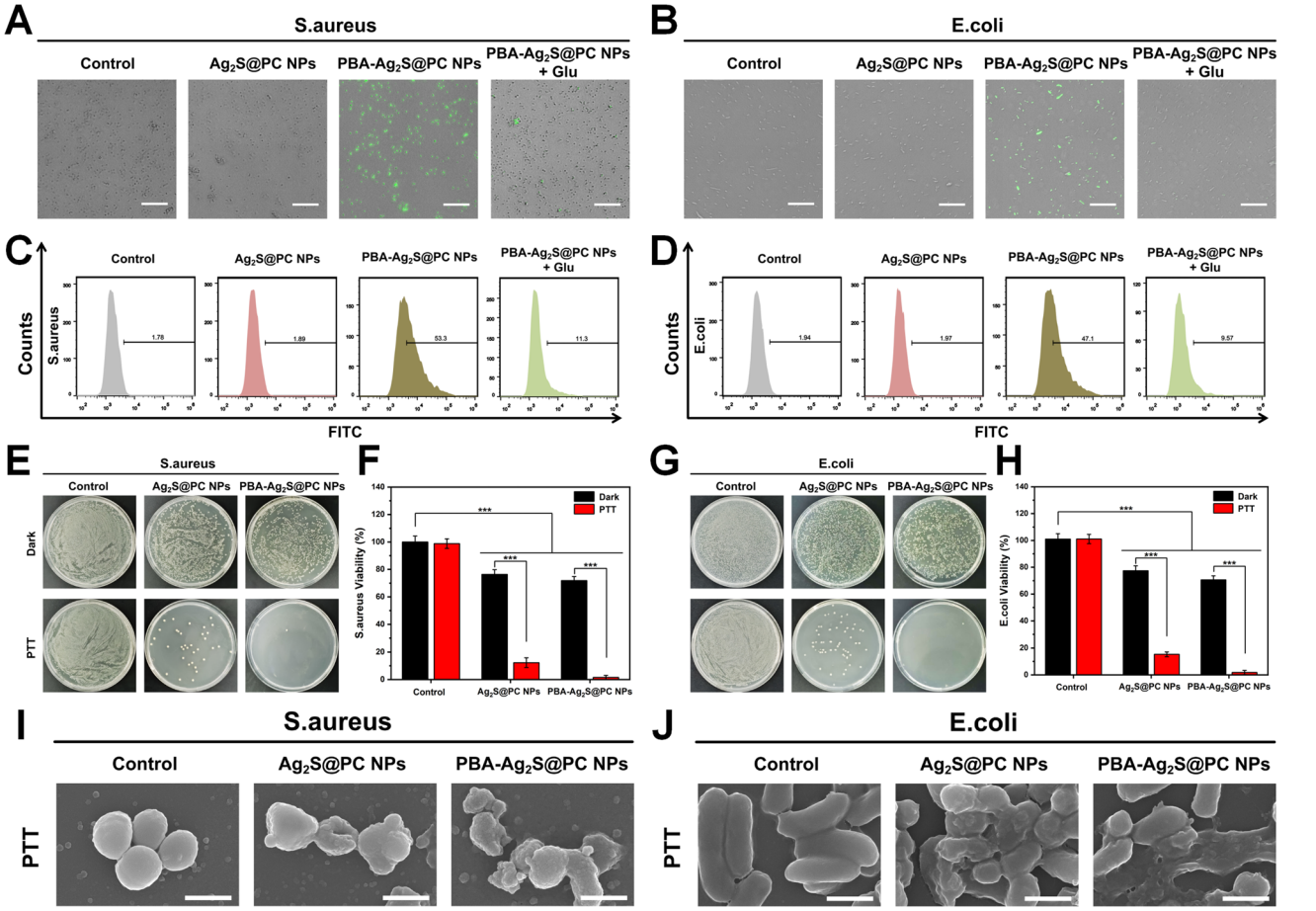

Fig. 4 The anti-bacterial effect of PBA-Ag_2S@PC NPs *in vitro*. (A and B) Representative fluorescence images of *S. aureus* and *E. coli* after incubating with FITC-labeled Ag_2S@PC NPs and PBA-Ag_2S@PC NPs, Scale = 20 μm. (C and D) Flow cytometric analysis of the bacterial positive rates following co-incubation of FITC-labeled Ag_2S@PC NPs and PBA-Ag_2S@PC NPs with *S. aureus* and *E. coli*, respectively. (E and G) Photographs of *S. aureus* and *E. coli* bacterial colonies after different treatments. (F and H) Statistical data of viability of *S. aureus* and *E. coli* ($n = 3$). ***$p < 0.001$. (I and J) SEM images of *S. aureus* and *E. coli* treated with various treatments under 808 nm laser irradiation, scale = 1 μm.

recorded. As illustrated in Fig. 5B and C, at various time points during treatment, all groups exhibited varying degrees of wound healing. Compared to the NS control group, both the Ag_2S@PC NPs treatment group and the PBA-Ag_2S@PC NPs treatment group demonstrated improved rates of wound healing. Furthermore, following adjunctive PPT therapy, both the Ag_2S@PC NPs + PTT treatment group and the PBA-Ag_2S@PC NPs + PTT treatment group showed a further reduction in wound area, with the PBA-Ag_2S@PC NPs + PTT treatment group exhibiting the most favorable wound healing outcomes. Specifically, at the conclusion of the treatment, the wound area in the NS control group was measured at 25.89 ± 3.14%. In contrast, the Ag_2S@PC NPs treatment group exhibited a wound area of 21.70 ± 2.17%, while the PBA-Ag_2S@PC NPs treatment group showed a reduction to 17.03 ± 1.30%. The Ag_2S@PC NPs combined with PTT resulted in an even smaller wound area of 12.72 ± 1.61%, and notably, the PBA-Ag_2S@PC NPs treatment group achieved a minimal wound area of just 7.32 ± 1.17%. The antibacterial activity of different treatment groups on infected wounds was evaluated using the plate counting method. On the fourth day of treatment, all groups exhibited varying degrees of bacterial residuals: the Ag_2S@PC NPs treatment group showed 77.53%, the PBA-Ag_2S@PC NPs treatment group demonstrated 64.11%, and the Ag_2S@PC NPs + PTT treatment group recorded a bacterial load of 15.65%. Notably, the PBA-Ag_2S@PC NPs + PTT treatment group had the lowest bacterial load at just 3.4% (Fig. 5D and E). The results indicate that PBA-Ag_2S@PC NPs possess significant potential for applications in targeted antibacterial synergistic PTT and promoting wound healing.

3.6. Histological evaluation of regenerated tissues

The healing and structural reconstruction of the epidermis and dermal tissue in each treatment group were observed using Hematoxylin and Eosin (H&E) staining, while Masson staining was employed to assess collagen deposition across the various treatment groups. The H&E results indicated that compared to the normal saline (NS) control group, all treatment groups exhibited varying degrees of wound length reduction and improvement in inflammatory cell infiltration on days 7 and 14 (Fig. 6A and C). Notably, the PBA-Ag_2S@PC NPs + PTT treatment group demonstrated the most significant healing effect, with

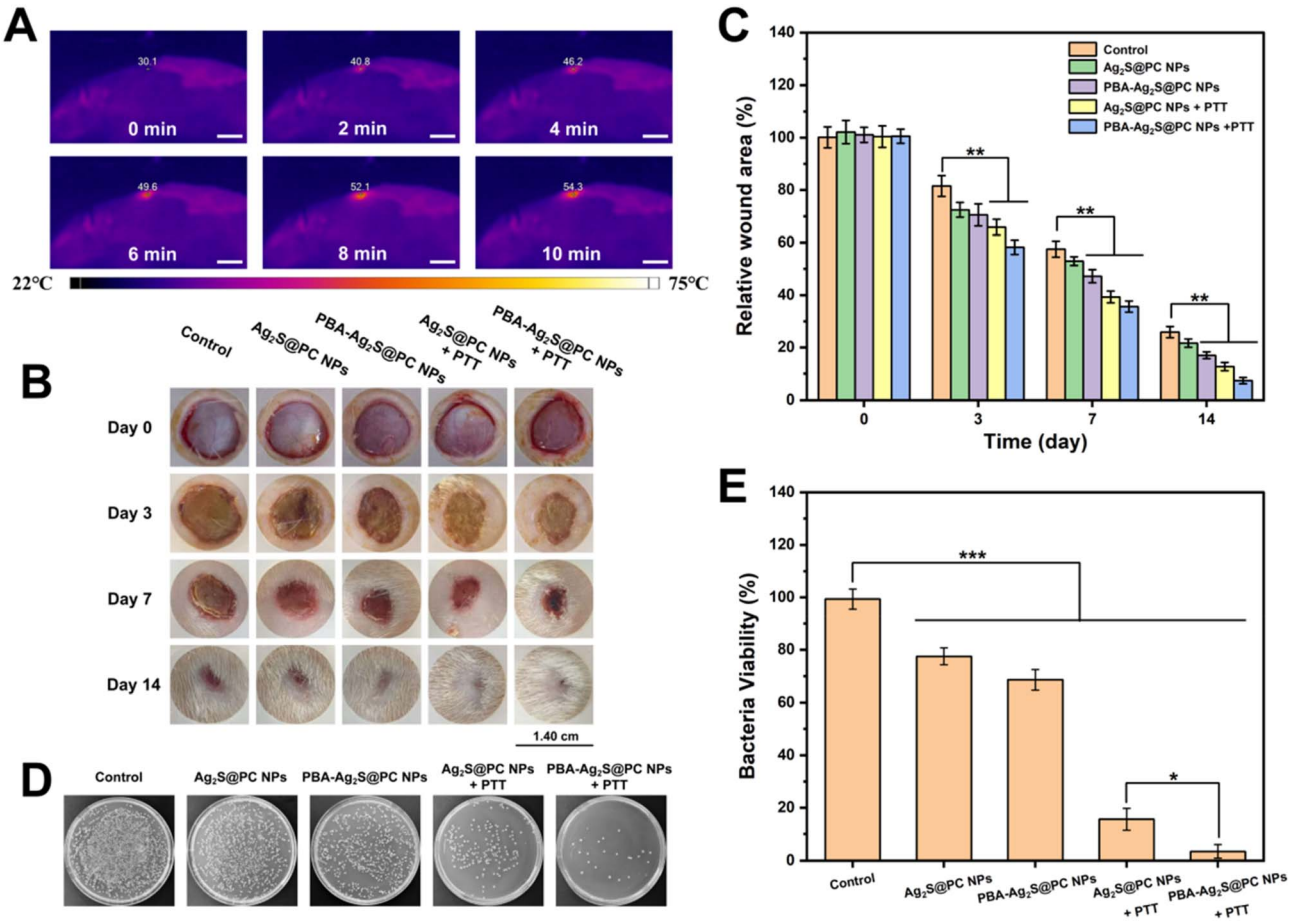

Fig. 5 The wound healing effect of PBA-Ag_2S@PC NPs *in vivo*. (A) Thermography of temperature changes in treating infected wounds with PBA-Ag_2S@PC NPs. (B) Photographs of the infected wound within 14 days. (C) Wound healing rates of *S. aureus* infected rats after various administration ($n = 6$). (D) Photographs of bacterial colonies of the wound tissues after various administration. (E) Bacteria viability of the wound tissues after various administration ($n = 3$). *$p < 0.05$. **$p < 0.01$. ***$p < 0.001$.

a greater presence of regenerated skin appendages. Masson staining results revealed that by day 7 post-modeling, all groups except for the NS control showed marked collagen fiber proliferation; this effect was most pronounced in the PBA-Ag_2S@PC NPs + PTT group. By day 14, all groups displayed varying levels of collagen deposition, with the highest accumulation observed in the PBA-Ag_2S@PC NPs + PTT group (Fig. 6B and D). These findings indicated that PBA-Ag_2S@PC NPs combined with photothermal therapy can effectively reduce bacterial load in wounds and accelerate the healing process of infected wounds, demonstrating the significant advantages of combining photothermal therapy with targeted therapy in promoting the recovery of infected wounds.

3.7. Biosafety of PBA-Ag_2S@PC NPs

The *in vivo* toxicity of PBA-Ag_2S@PC NPs was further evaluated. Compared to the healthy control group, no significant tissue damage was observed in the major organs (liver, heart, spleen, lungs, and kidneys) of the treatment groups receiving PBA-Ag_2S@PC NPs and PBA-Ag_2S@PC NPs + NIR (Fig. S9). Biochemical indicators related to liver and kidney function remained within normal ranges, with no signs of acute liver or kidney injury detected (Fig. S10). These results confirm that PBA-Ag_2S@PC NPs possess good biosafety for *in vivo* antibacterial therapy.

3.8. Discussion and limitation

This study integrates PBA- and PC-modified Ag_2S nanocomposites for synergistic bacterial-targeted therapy and photothermal therapy against *Staphylococcus aureus*-infected wounds. The results demonstrated their excellent bacterial targeting capability, potent photothermal antibacterial activity, favorable biocompatibility, and significant wound-healing promotion effect. These advantageous properties render the nanocomposites highly promising for trauma management—particularly in accelerating the healing of infected wounds—and provide both theoretical insights and practical foundations for developing novel functional wound dressings.

However, this study has several limitations. First, numerous studies have demonstrated that PBA and its derivatives exhibit certain kinetic preferences toward bacterial targets *in vivo*.[44,45] Although our results show that PBA-Ag_2S@PC NPs selectively

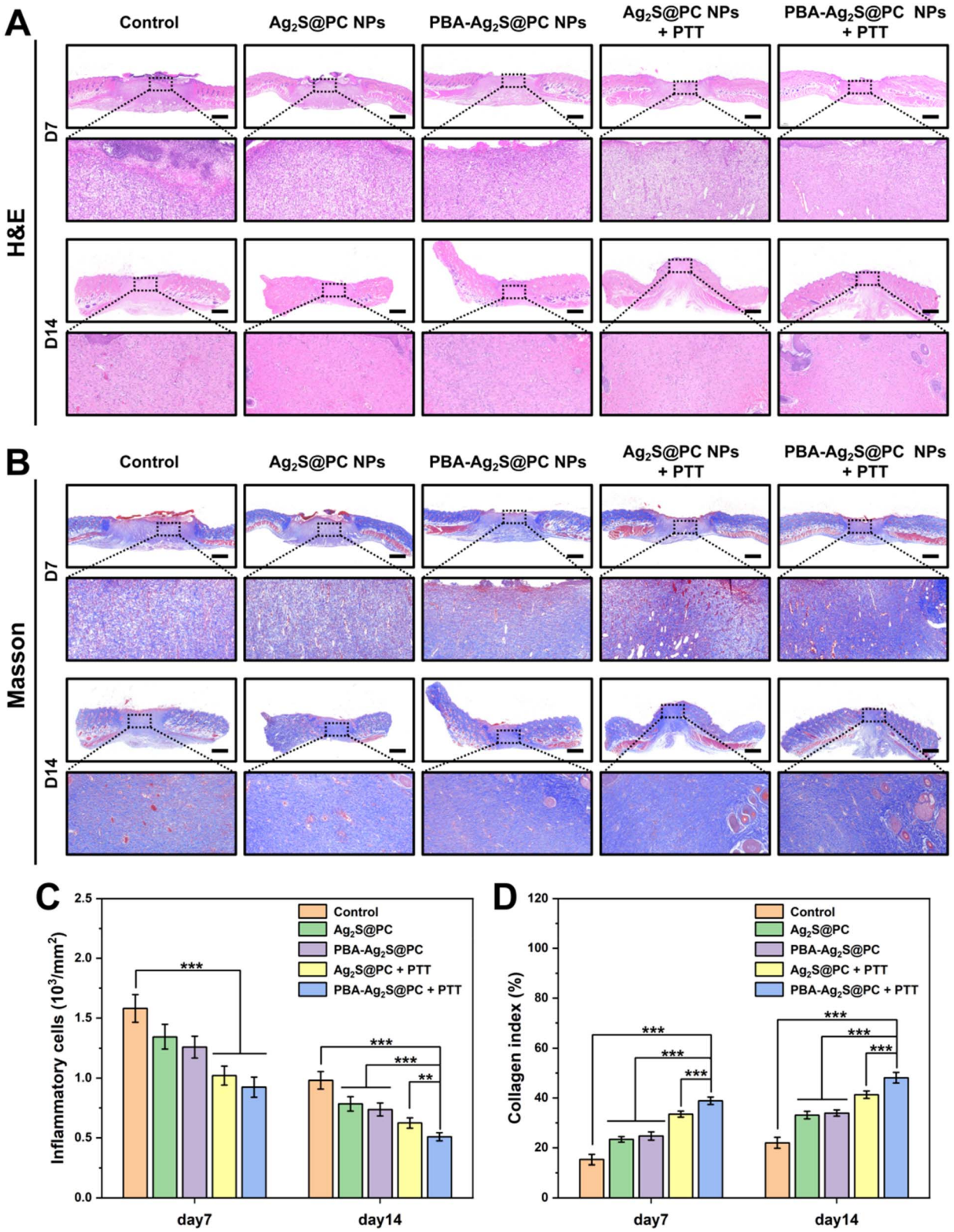

Fig. 6 Results of histological analysis. The representative H&E (A) and Masson staining (B) images of the peri-implant tissues on day 7 and day 14, scale = 1 mm. (C) Quantitative analysis of the inflammatory cells from the H&E staining images ($n = 3$). (D) Quantitative analysis of the collagen deposition from Masson's trichrome-stained tissues staining images ($n = 3$). $^{**}p < 0.01$. $^{***}p < 0.001$.

accumulate on bacterial surfaces *in vivo*, the extent and specificity of their binding to host cells remain insufficiently characterized. Second, given that *S. aureus* is the most representative pathogen in skin and soft-tissue infections, this study focused exclusively on Gram-positive bacteria *in vivo*; investigations involving Gram-negative bacteria *in vivo* are warranted in future work. Third, in actual infected wounds, the presence of bacterial biofilms and exudative proteins may interfere—albeit to an uncertain degree—with nanoparticle binding and subsequent photothermal antibacterial efficacy. Fourth, while the *in vivo* wound-healing performance and acute toxicity of PBA-Ag_2S@PC NPs were evaluated, their *in vivo* pharmacokinetics, biodistribution, long-term biocompatibility, and systemic biosafety require further comprehensive investigation. Looking ahead, future studies could extend the application of PBA-Ag_2S@PC NPs to other acute or chronic wound models (including burn wounds and diabetic wounds) and integrate molecular biological approaches to mechanistically elucidate how these nanoparticles promote tissue repair and regeneration.

4 Conclusion

In summary, we have developed a multifunctional nanoplatform (PBA-Ag_2S@PC NPs) for bacterial targeting photothermal therapy and promotion wound healing. This platform is composed of the targeting fragment PBA, the photothermal agent Ag_2S, and the nano stabilizer PC. Firstly, PBA-Ag_2S@PC NPs exhibit remarkable photothermal conversion capabilities and enhance the antibacterial effects of photothermal therapy through targeted bacterial interaction. Furthermore, PBA-Ag_2S@PC NPs demonstrate low cytotoxicity and good blood compatibility. *In vivo* experiments confirm the excellent potential for promoting healing in infected wounds. Overall, PBA-Ag_2S@PC NPs provide a novel approach for the development of targeted photothermal therapeutic nanomedicines and hold significant promise for applications in skin wound repair.

Ethics approval and consent to participate

Animal experiments were conducted with approval from the Ethical Committee of Animal Experiments of South Medical University (IACUC-LAC-20251113-006) and according to the Committee Guidelines.

Author contributions

Yixiang HePeng: data curation, writing – original draft writing. Zhi Xu: data curation, formal analysis, methodology, writing – original draft writing. Ping Gou: data curation, writing – original draft writing. Bosong Zhou: data curation, investigation. Quan Zheng: data curation, investigation. Ke Zhu: data curation, investigation. Xiangfeng Liu: data curation, investigation. Ruiyuan Liu: conceptualization, resources, supervision, validation, writing – review & editing. Xu Wu: conceptualization, funding acquisition, resources, supervision, validation, writing – review & editing. Chao Zhang: resources, supervision, validation, writing – review & editing.

Conflicts of interest

The authors declare no conflict of interest.

Data availability

The data that support the findings of this study are available in the supplementary information (SI) material of this article. Supplementary information is available. See DOI: https://doi.org/10.1039/d5ra09845a.

Acknowledgements

This work was financially supported by Marine Economy Development Special Fund (Six Marine Industries) under the Department of Natural Resources of Guangdong Province (GDNRC [2024]27).

References

1 M. Falcone, B. De Angelis, F. Pea, A. Scalise, S. Stefani, R. Tasinato, O. Zanetti and L. Dalla Paola, Challenges in the management of chronic wound infections, *J. Global Antimicrob. Resist.*, 2021, **26**, 140–147, DOI: 10.1016/j.jgar.2021.05.010.

2 P. Kolimi, S. Narala, D. Nyavanandi, A. A. A. Youssef and N. Dudhipala, Innovative Treatment Strategies to Accelerate Wound Healing: Trajectory and Recent Advancements, *Cells*, 2022, **11**(15), 2439, DOI: 10.3390/cells11152439.

3 M. A. Cook and G. D. Wright, The past, present, and future of antibiotics, *Sci. Transl. Med.*, 2022, **14**(657), eabo7793, DOI: 10.1126/scitranslmed.abo7793.

4 T. Pulingam, T. Parumasivam, A. M. Gazzali, A. M. Sulaiman, J. Y. Chee, M. Lakshmanan, C. F. Chin and K. Sudesh, Antimicrobial resistance: Prevalence, economic burden, mechanisms of resistance and strategies to overcome, *Eur. J. Pharm. Sci.*, 2022, **170**, 106103, DOI: 10.1016/j.ejps.2021.106103.

5 B. Singh, A. Bhat and K. Ravi, Antibiotics Misuse and Antimicrobial Resistance Development in Agriculture: A Global Challenge, *Environ. Health*, 2024, **2**(9), 618–622, DOI: 10.1021/envhealth.4c00094.

6 B. A. Omran, B. S. Tseng and K. H. Baek, Nanocomposites against Pseudomonas aeruginosa biofilms: Recent advances, challenges, and future prospects, *Microbiol. Res.*, 2024, **282**, 127656, DOI: 10.1016/j.micres.2024.127656.

7 Y. Wang, W. Du, T. Zhang, Y. Zhu, Y. Ni, C. Wang, F. M. Sierra Raya, L. Zou, L. Wang and G. Liang, A Self-Evaluating Photothermal Therapeutic Nanoparticle, *ACS Nano*, 2020, **14**(8), 9585–9593, DOI: 10.1021/acsnano.9b10144.

8 Q. Wang, D. Zhang, Y. Qi, C. Huang, D. Ding and C. Liu, Multifunctional PdH-hydride MOFs for synergistic hydrogen and photothermal antibacterial therapy in accelerated wound healing, *Front. Pharmacol*, 2025, **16**, 1587890, DOI: 10.3389/fphar.2025.1587890.

9 Y. Yu, R. Tian, Y. Zhao, X. Qin, L. Hu, J. J. Zou, Y. W. Yang and J. Tian, Self-Assembled Corrole/Chitosan Photothermal Nanoparticles for Accelerating Infected Diabetic Wound Healing, *Adv. Healthcare Mater.*, 2023, **12**(16), e2201651, DOI: 10.1002/adhm.202201651.

10 S. Lin, H. Chen, R. Wang, T. Jiang, R. Wang and F. Yu, Hollow silver-gold alloy nanoparticles for enhanced photothermal/photodynamic synergetic therapy against bacterial infection and acceleration of wound healing, *Biomater. Sci.*, 2023, **11**(14), 4874–4889, DOI: 10.1039/d3bm00567d.

11 H. Shen, C. Zhang, Y. Meng, Y. Qiao, Y. Ma, J. Chen, X. Wang and L. Pan, Biomimetic Hydrogel Containing Copper Sulfide Nanoparticles and Deferoxamine for Photothermal Therapy of Infected Diabetic Wounds, *Adv. Healthcare Mater.*, 2024, **13**(8), e2303000, DOI: 10.1002/adhm.202303000.

12 P. Sun, K. Li, X. Liu, J. Wang, X. Qiu, W. Wei and J. Zhao, Peptide-mediated Aqueous Synthesis of NIR-II Emitting Ag_2S Quantum Dots for Rapid Photocatalytic Bacteria Disinfection, *Angew Chem. Int. Ed. Engl.*, 2023, **62**(14), e202300085, DOI: 10.1002/anie.202300085.

13 X. Zhou, Z. Meng, J. She, *et al.*, Near-Infrared Light-Responsive Nitric Oxide Delivery Platform for Enhanced Radioimmunotherapy, *Nano-Micro Lett.*, 2020, **12**(1), 100, DOI: 10.1007/s40820-020-00431-3.

14 J. Zhao, Q. Zhang, W. Liu, G. Shan and X. Wang, Biocompatible BSA-Ag2S nanoparticles for photothermal therapy of cancer, *Colloids Surf., B*, 2022, **211**, 112295, DOI: 10.1016/j.colsurfb.2021.112295.

15 G. Ma, X. Zhang, K. Zhao, S. Zhang, K. Ren, M. Mu, C. Wang, X. Wang, H. Liu, J. Dong and X. Sun, Polydopamine Nanostructure-Enhanced Water Interaction with pH-Responsive Manganese Sulfide Nanoclusters for Tumor Magnetic Resonance Contrast Enhancement and Synergistic Ferroptosis-Photothermal Therapy, *ACS Nano*, 2024, **18**(4), 3369–3381, DOI: 10.1021/acsnano.3c10249.

16 A. Shetty, H. Lang and S. Chandra, Metal Sulfide Nanoparticles for Imaging and Phototherapeutic Applications, *Molecules*, 2023, **28**(6), 2553, DOI: 10.3390/molecules28062553.

17 A. M. Paca and P. A. Ajibade, Metal Sulfide Semiconductor Nanomaterials and Polymer Microgels for Biomedical Applications, *Int. J. Mol. Sci.*, 2021, **22**(22), 12294, DOI: 10.3390/ijms222212294.

18 Q. Yu, C. Wang, X. Zhang, H. Chen, M. X. Wu and M. Lu, Photochemical Strategies toward Precision Targeting against Multidrug-Resistant Bacterial Infections, *ACS Nano*, 2024, **18**(22), 14085–14122, DOI: 10.1021/acsnano.3c12714.

19 X. Qie, M. Zan, P. Gui, H. Chen, J. Wang, K. Lin, Q. Mei, M. Ge, Z. Zhang, Y. Tang, W. F. Dong and Y. Song, Design, Synthesis, and Application of Carbon Dots With Synergistic Antibacterial Activity, *Front. Bioeng. Biotechnol.*, 2022, **10**, 894100, DOI: 10.3389/fbioe.2022.894100.

20 X. Wang, W. Shi, Y. Jin, Z. Li, T. Deng, T. Su, A. Zheng and L. Cao, Photodynamic and photothermal bacteria targeting nanosystems for synergistically combating bacteria and biofilms, *J. Nanobiotechnol.*, 2025, **23**(1), 40, DOI: 10.1186/s12951-025-03126-2.

21 S. Zhou, L. Dai, L. Pan, G. Shen and Z. Qian, Phenylboronic acid-modified nanoparticles for cancer treatment, *Chem. Commun.*, 2025, **61**(24), 4595–4605, DOI: 10.1039/d4cc06730d.

22 A. K. Jangid and K. Kim, Phenylboronic acid-functionalized biomaterials for improved cancer immunotherapy *via* sialic acid targeting, *Adv. Colloid Interface Sci.*, 2024, **333**, 103301, DOI: 10.1016/j.cis.2024.103301.

23 Y. Zhang, M. Wu, W. Dai, M. Chen, Z. Guo, X. Wang, D. Tan, K. Shi, L. Xue, S. Liu and Y. Lei, High drug-loading gold nanoclusters for responsive glucose control in type 1 diabetes, *J. Nanobiotechnol.*, 2019, **17**(1), 74, DOI: 10.1186/s12951-019-0505-z.

24 L. Liu, X. Wang, S. Zhu, C. Yao, D. Ban, R. Liu, L. Li and S. Wang, Controllable Targeted Accumulation of Fluorescent Conjugated Polymers on Bacteria Mediated by a Saccharide Bridge, *Chem. Mater.*, 2019, **31**(23), 9882–9889, DOI: 10.1021/acs.chemmater.9b04034.

25 L. Wang, W. Zheng, L. Zhong, Y. Yang, Y. Chen, Q. Hou, P. Yu and X. Jiang, Phenylboronic Acid-Modified Gold Nanoclusters as a Nanoantibiotic to Treat Vancomycin-Resistant Enterococcus faecalis-Caused Infections, *ACS Nano*, 2023, **17**(20), 19685–19695, DOI: 10.1021/acsnano.3c02886.

26 H. Wang, W. You, B. Wu, *et al.*, Phenylboronic acid-functionalized silver nanoparticles for highly efficient and selective bacterial killing, *J. Mater. Chem. B*, 2022, **10**(15), 2844–2852, DOI: 10.1039/d2tb00320a.

27 J. Liu, W. He, Z. Liu, H. He, H. Gan, M. Hu, X. Zhao, G. Xie, B. Chang and N. Guo, Self-delivery nanomedicine for targeted antibacterial and anti-inflammatory therapy of subcutaneous skin infection, *ACS Appl. Nano Mater.*, 2025, **8**(13), 6288–6300, DOI: 10.1021/acsanm.4c06585.

28 Y. Liu, Q. Lan, J. Liu, Y. Shi, Q. Wu, Q. Wang, S. Yang and F. Cheng, Phenylboronic acid-functionalized BSA@CuS@PpIX nanoparticles for enhanced antibacterial photodynamic/photothermal therapy, *J. Drug Delivery Sci. Technol.*, 2023, **88**, 104965, DOI: 10.1016/j.jddst.2023.104965.

29 Z. Li, Z. Zhao, S. Chen, W. Wu, Y. Jin, J. Mao, Y. Lin and Y. Jiang, Chemically Tailored Single Atoms for Targeted and Light-Controlled Bactericidal Activity, *Adv. Healthcare Mater.*, 2024, **13**(5), e2302480, DOI: 10.1002/adhm.202302480.

30 Z. Xu, Y. Jin, C. Zhang, Y. HePeng, S. Yang, X. Chen, K. Qu, Q. Ning, M. Kourouma, X. Li, R. Liu and X. Wu, A methacrylated pullulan hydrogel incorporating phycocyanin-functionalized copper sulfide nanoparticles for photothermal antibacterial therapy and improved

wound healing, *Int. J. Biol. Macromol.*, 2025, **315**(Pt 1), 144446, DOI: 10.1016/j.ijbiomac.2025.144446.

31 J. Dong, Y. Lang, J. He, J. Cui, X. Liu, H. Yuan, L. Li, M. Zhou and S. Wang, Phycocyanin-based multifunctional microspheres for treatment of infected radiation-induced skin injury, *Biomaterials*, 2025, **317**, 123061, DOI: 10.1016/j.biomaterials.2024.123061.

32 Z. Xu, Y. Jin, Z. Zhang, Y. HePeng, C. Zhang, S. Yang, K. Qu, Q. Ning, M. Kourouma, R. Liu, X. Wu and X. Li, Phycocyanin functionalized selenium nanoparticles for type I photodynamic antibacterial therapy and wound healing, *J. Mater. Chem. B*, 2025, **13**(27), 8208–8218, DOI: 10.1039/d5tb00716j.

33 C. Liu, Y. Fu, C. E. Li, T. Chen and X. Li, Phycocyanin-Functionalized Selenium Nanoparticles Reverse Palmitic Acid-Induced Pancreatic β Cell Apoptosis by Enhancing Cellular Uptake and Blocking Reactive Oxygen Species (ROS)-Mediated Mitochondria Dysfunction, *J. Agric. Food Chem.*, 2017, **65**(22), 4405–4413, DOI: 10.1021/acs.jafc.7b00896.

34 A. Fakouri, M. Mahmoudifard, N. Ghorbani, M. Shafiei and K. A. Noghabi, Natural-synthetic hybrid nanoparticles: Polydopamine-Phycocyanin composites for enhanced antibacterial phototherapy against bacterial pathogens, *J. Photochem. Photobiol., B*, 2025, **270**, 113222, DOI: 10.1016/j.jphotobiol.2025.113222.

35 Y. You, S. Cheng, L. Zhang, Y. Zhu, C. Zhang and Y. Xian, Rational Modulation of the Luminescence of Upconversion Nanomaterials with Phycocyanin for the Sensing and Imaging of Myeloperoxidase during an Inflammatory Process, *Anal. Chem.*, 2020, **92**(7), 5091–5099, DOI: 10.1021/acs.analchem.9b05468.

36 Y. Li, Z. Zhang and A. Abbaspourrad, Improved pH stability, heat stability, and functionality of phycocyanin after PEGylation, *Int. J. Biol. Macromol.*, 2022, **222**(Pt B), 1758–1767, DOI: 10.1016/j.ijbiomac.2022.09.261.

37 H. Tian, Z. Zhang, F. Ning, W. Li, X. Sun, X. Yang and L. Luo, Effect of ultrasound pretreatment complex glycation on the structure and functional activity of phycocyanin modified by mannose, *LWT–Food Sci. Technol.*, 2023, **188**, 115390, DOI: 10.1016/j.lwt.2023.115390.

38 Z. Li, C. Qian, X. Zheng, X. Qi, J. Bi, H. Wang and J. Cao, Collagen/chitosan/genipin hydrogel loaded with phycocyanin nanoparticles and ND-336 for diabetic wound healing, *Int. J. Biol. Macromol.*, 2024, **266**(Pt 1), 131220, DOI: 10.1016/j.ijbiomac.2024.131220.

39 R. Zhang, L. Wang, L. Meng, W. Shang, Y. Ren, Q. Qi, J. Liu, B. Cui, Z. Meng, X. Jiang, L. Ding, Y. Gou, Y. He, Q. Zhang and C. Ren, A slime-inspired phycocyanin/κ-carrageenan-based hydrogel bandage with ultra-stretchability, self-healing, antioxidative, and antibacterial activity for wound healing, *Int. J. Biol. Macromol.*, 2025, **289**, 138786, DOI: 10.1016/j.ijbiomac.2024.138786.

40 R. Arora, J. Dhaliwal, N. Dhaliwal, N. Thakur, S. Kesavaraja and K. Chopra, Topical application of phycocyanin accelerates wound healing in STZ-induced diabetic rats *via* activation of the Nrf2 signaling pathway, *3 Biotech*, 2025, **15**(9), 312, DOI: 10.1007/s13205-025-04438-8.

41 J. Qu, X. Geng, S. Qin, J. Li and W. Li, The utilization of TGase-crosslinked phycocyanin-collagen hydrogels for the purpose of facilitating skin wound healing, *Int. J. Biol. Macromol.*, 2025, **320**(Pt 3), 145932, DOI: 10.1016/j.ijbiomac.2025.145932.

42 W. Gong, H. B. Huang, X. C. Wang, W. Y. He and J. N. Hu, Coassembly of Fiber Hydrogel with Antibacterial Activity for Wound Healing, *ACS Biomater. Sci. Eng.*, 2023, **9**(1), 375–387, DOI: 10.1021/acsbiomaterials.2c00716.

43 S. Xi, H. Xiao, Z. Duan, L. Li, J. Chen, T. Hu, X. Li, L. Hu and R. Liu, Effective One-for-All Phototheranostic Agent for Hypoxia-Tolerant NIR-II Fluorescent/PA Image-Guided Phototherapy, *Small*, 2025, **21**(7), e2406226, DOI: 10.1002/smll.202406226.

44 Y. Zhang, Y. Deng, C. Su, K. Wu, C. Li, J. Wang, H. Zhang, D. Luo, S. Huang, L. Zhao, M. Xiong and Y. Bao, A conjugate strategy capable of targeting bacteria and selectively being activated at infection sites, *Sci. China Mater.*, 2025, **68**(6), 2132–2142, DOI: 10.1007/s40843-025-3360-x.

45 Y. Chen, A. Liu, B. Yang, Z. Li, B. Ye, Z. Guo, Z. Liu and H. Chen, Photoluminescence and photothermal conversion in boric acid derived carbon dots for targeted microbial theranostics, *Chin. Chem. Lett.*, 2024, **35**(9), 109295, DOI: 10.1016/j.cclet.2023.109295.